the statistical manipulation of SPECT images after reconstruction and anatomical standardization makes it easier for a radiologist to detect subtle changes.[6,7,9] The Z-score of three-dimensional stereotactic surface projection (3DSSP) images also adds information regarding cortical perfusion even in very early stages of AD.[10–12]

The receiver-operating characteristics (ROC) analysis by human observers is often used to assess the benefits of newly developed diagnostic techniques.[8–11] Conventionally, interpretation by human observers has been the standard for assessing the detection performance of any algorithm. However, human-observer studies are difficult and time-consuming. Therefore, an alternative method using a mathematical "model," such as a channelized Hotelling (CH) observer, has been developed to assess the effect of image processing (e.g., filter cutoff frequency and scatter compensation strategies).[13–18] A CH observer is characterized as having a psychophysiologic basis in the frequency-selective channels of the human visual system and is expected to predict human performance in image interpretation.[14]

A good agreement between the CH observer (or a similar numerical model) and a human observer for myocardial and hepatic SPECT imaging was reported previously.[18–21] Sankaran et al. reported that the reference index for the performance of defect detection, that is, the area under the ROC curve (Az), is slightly higher for the CH observer than for the human observer, but was marginally within 1 S.D. of human Az for all combinations of attenuation, detector response, and scatter corrections for myocardial SPECT images.[18] Gifford et al. reported that the CH observer in tumor detection by ^{67}Ga SPECT gives a good quantitative agreement with human data sets obtained from two image reconstruction strategies, Filtered-Back Projection (FBP) and Order Subset Expectation Maximization (OS-EM).[21] These studies were aimed at evaluating the diagnostic accuracy of a CH observer compared with a human observer for different image reconstruction and processing protocols. The results suggest that a CH observer may be used as an approximation of a human observer for various detection tasks. The CH observer, however, has not been validated for the assessment of statistically processed brain perfusion images.

The goal of this study was to compare human and CH observers through ROC curves to detect the perfusion pattern characteristic of AD on SPECT images. In this study, we investigated the effects of three frequency cutoff channel models of CH observers.

MATERIAL AND METHODS

Subjects

Brain perfusion SPECT images of 52 subjects were analyzed (AD patients, n = 21; healthy volunteers as controls, n = 31). In the patient group, there were 6 males and 15 females, with a mean age of 69.3 ± 6.3 years (range, 51–75). They were clinically diagnosed by geriatric physicians as having probable AD on the basis of NINCDS-ADRDA criteria.[22] Their averaged Mini Mental State Examination (MMSE) score was 21.6 ± 2.1 (range, 17–26).[23] The controls comprised 15 males and 16 females, with a mean age of 64.9 ± 6.27 years (range 54–74). They were participants in a research program on brain aging in city dwellers conducted by the Institute of Development,

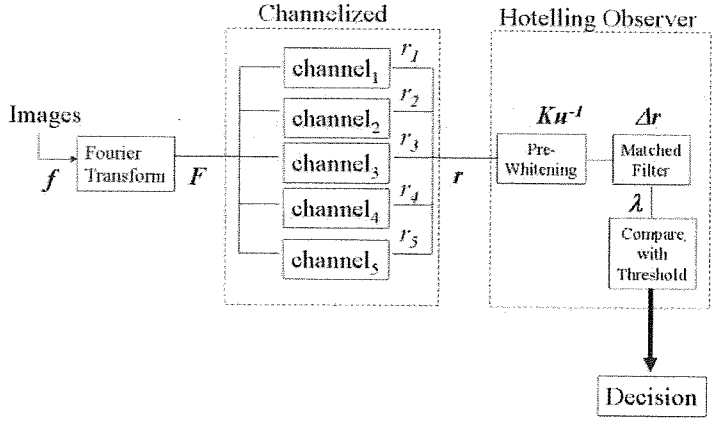

Fig. 1 Schematic diagram of a CH observer. Image **f** was first converted by Fourier transformation. In frequency domain, filtering was applied for Fourier transformed image **F** using radially symmetric channels $\mathbf{u}_c$ and then the channel matrix **r** was obtained (named as Channelized process). The channel matrix **r** was processed by pre-whitening ($\mathbf{K}_U^{-1}$) and matched filter ($\Delta\mathbf{r}$) and then finally, test statistic λ was obtained. The test statistic λ was diagnosed using threshold λ_{thresh}, whether the input image **f** falls in one group or the other (named as Hotelling observer process). Character of Hotelling observer is the use of averaged matrix from the two-covariance matrices derived from channel matrices for one group or the other for $\mathbf{K}_U$ matrix.

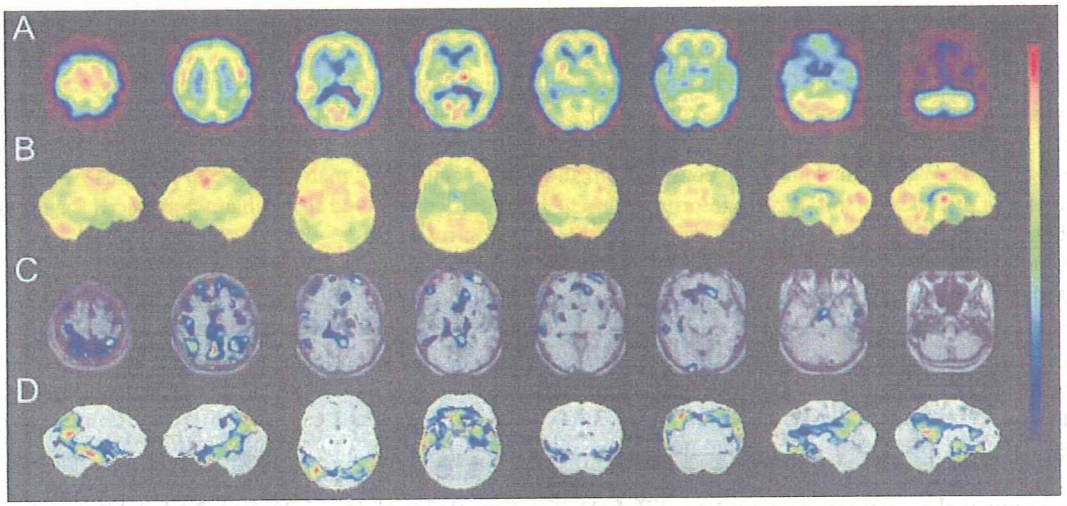

Fig. 2 Representative SPECT images (A), 3DSSP images (B), Z-scores of SPECT images (C) and Z-scores of 3DSSP images (D) used for image interpretation experiment. Images in (B) and (D) are, from left to right, right lateral, left lateral, superior, inferior, anterior, posterior, right mid-sagittal, and left mid-sagittal views. Images in (C) and (D) were superimposed on template MR images.

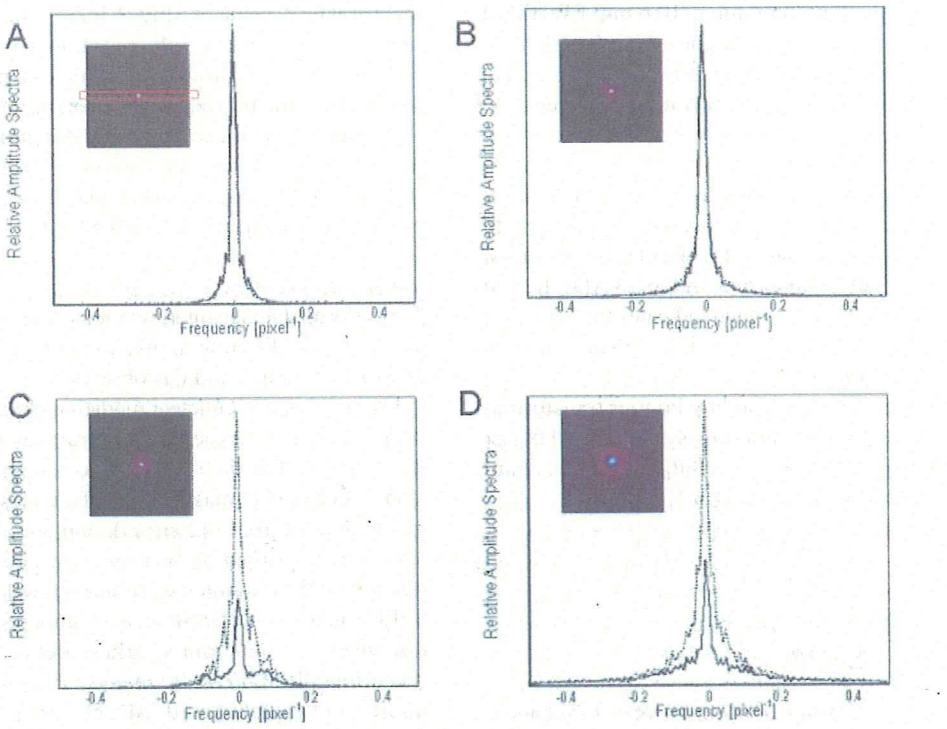

Fig. 3 Profiles of Fourier amplitude spectra from normal control (*solid line*) and Alzheimer's dementia patient (*dotted line*) calculated from SPECT image (A), 3DSSP image (B), Z-score of SPECT image (C) and Z-score of 3DSSP image (D). Individual profiles for the four types of image were obtained from the following images: images in (A) and (C) are transverse views at central slices of 3D Fourier amplitude spectra. Images in (B) and (D) are summed 2D Fourier amplitude spectra along eight individual slices of 3DSSP images.

Aging and Cancer, Tohoku University and there were no abnormalities on their MR images.[24] In this study, we randomly selected 10 controls (mean age, 64.8 ± 5.65 years) as the normal database for the calculation of Z-score, and the other 21 controls were used as test subjects for ROC analysis. We obtained informed consent from all AD patients or their next of kin. Written informed consent was obtained from all controls after a proper explanation of the study, in accordance with the Code of Ethics of the World Medical Association (Declaration of Helsinki).

SPECT study

SPECT study of cerebral perfusion was performed using *N*-isopropyl-[^{123}I]*p*-iodoamphetamine (IMP). All subjects received 111 MBq of the compound intravenously under standard resting conditions while lying supine on a scanning couch. The main projection data (158 keV ± 15%, 4 degree sampling) were acquired continuously for 30 min using a triple-head SPECT camera (Multispect3, Siemens, Malvern, PA, USA) with fan-beam collimators. The projection data were smoothed using a Butterworth filter (order 8 and a cutoff of 0.3 cycles/pixel) and reconstructed by FBP with a Ramp filter (10.6 mm FWHM of image resolution). Attenuation correction by Chang's method was applied assuming an attenuation coefficient of 0.08 cm^{-1}. Scatter correction was not performed.

Channelized Hotelling observer

A schematic diagram of CH observer is shown in Figure 1. CH observer accepts as an input an image f belonging to either a class of normal images, f_B, or a class of abnormal images (in this study, "abnormal" refers to AD), f_L, and provides the test statistic λ, which indicates the statistical index that determines whether the input image f falls in one group or the other.[13,14]

Initially, image f is converted by Fourier transformation. In frequency domain, filtering is applied for Fourier transformed image F (ρ) using radially symmetric channels $u_c(\rho)$ defined by the formula [21]

$$u_c(\rho) = \begin{cases} 1 \parallel \rho \parallel \in [\rho_0 2^{c-1}, \rho_0 2^c) \\ 0 \quad \text{Otherwise} \end{cases},$$

$$r_c = \frac{\sum_\rho u_c(\rho) \cdot F(\rho)}{\sum_\rho u_c(\rho)} \qquad (1)$$

for c ∈{1,2,3,4,5}. By this filtering process, the channel matrix **r** (= [r_1, . . . , r_c]) is obtained. In this study, sets with the frequency cutoff ρ_0 (0.015, 0.02313, and 0.03125 pixel^{-1}) were tested. These were designated as the low-, mid-, and high-ρ_0 channel models, respectively. The cutoff ρ_0 values of 0.015 and 0.03125 were obtained from Gifford et al.[21] and Wollenweber et al.,[19] respectively, and 0.02313 is the mean of these two values. The test statistic λ of a CH observer for the task of detecting AD is as follows:

$$\lambda(\mathbf{f}) = \left[\overline{r_L} - \overline{r_B}\right]^T \mathbf{K_U}^{-1}\mathbf{r}, \qquad (2)$$

where r_L and r_B are the means of the two classes of channel matrices for the AD and control groups, respectively. The script "T" denotes a matrix transposition, and K_U is the c × c matrix averaged from the two-covariance matrices derived from channel matrices for the AD and control groups.

Image processing

As shown in Figure 2, we generated four types of images. A) SPECT images: After anatomical standardization by SPM 99, the normalization of global counts for each subject was set to 500 with proportional scaling. The matrix size of a SPECT image was 79 × 95 × 68 (2 × 2 × 2 mm^3). B) 3DSSP images: 3DSSP images (128 × 128; pixel size, 2.25 × 2.25 mm^2; and eight (projection) images) were processed according to a previous report,[12] where the maximum cortical activity was extracted adjacent to predefined surface pixels on a pixel-by-pixel basis, and the normalization of global counts for each subject was set to 500 with proportional scaling. C) Z-score images: The Z-value of SPECT images was calculated on a pixel-by-pixel basis with the following equation using SPECT images: Z = (mean of normalized pixel of normal database – normalized pixel of a patient)/SD of database. The normal database consisted of 10 controls as described in the previous section. D) Z-score of 3DSSP images: Z-score of 3DSSP images was calculated on a pixel-by-pixel basis using the equation described in C).

Image interpretation

We performed image interpretation using the four types of image for the differential diagnosis of AD patients from controls by human and CH observers.

Five experienced nuclear medicine physicians (4, 6, 8, 9, and 18 years of experience in brain nuclear medicine) were involved in the following four interpretation sessions: A) SPECT images: SPECT images in transverse (48 slices), sagittal (42 slices), and coronal planes (42 slices) were printed on two separate sheets. B) 3DSSP images: 3DSSP images were interpreted together with SPECT images. A 3DSSP image comprised eight projection images of the brain's surface and was printed on a sheet (Fig. 2B). C) Z-score images: Z-score images were interpreted together with SPECT images. A Z-score image (z ≥ 1) superimposed upon template MR images (Fig. 2C) was printed on two sheets in transverse, sagittal, and coronal planes. D) Z-score of 3DSSP images: Z-scores of 3DSSP images were interpreted together with SPECT and 3DSSP images. A Z-score of 3DSSP image (z ≥ 1) superimposed on a template MR image (Fig. 2D) was printed on a sheet. The nuclear medicine physicians were unaware of subject information or of predicted results, except for the information that the subjects comprised aged normal and AD patients. At the beginning of the

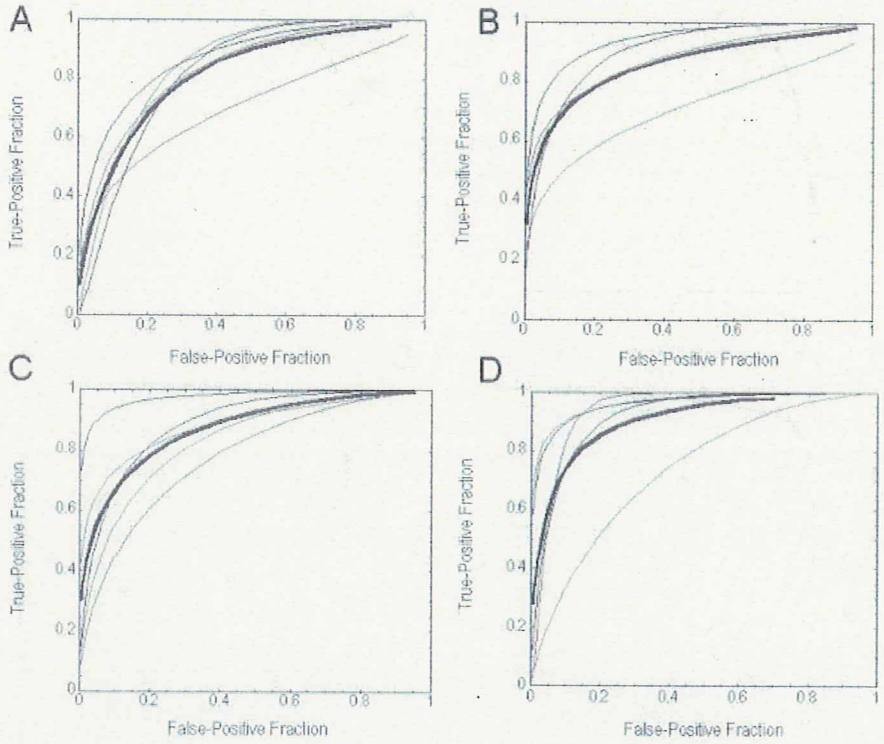

Fig. 4 Averaged (*bold solid lines*) and individual physician's (*thin solid lines*) ROC curves obtained from SPECT images (A), 3DSSP images (B), Z-scores of SPECT images (C) and Z-scores of 3DSSP images (D).

interpretation study, the nuclear medicine physicians received lectures, and practiced on one normal SPECT study and one study of a patient. The studies were not included in the study materials. Allotted time for the lecture and practice was 30 minutes in total. The lecture explained the typical SPECT findings in AD. The criteria were hypoperfusion of bilateral posterior cingulate gyri and precunei and/or hypoperfusion of bilateral medial-temporal and temporo-parietal lobes. Images were evaluated on a five-point scale of certainty: definitely, possibly, equivocally, possibly not, and definitely not. To avoid crossover interpretation artifacts, only one set of images was interpreted per session.

For the CH observer, the test statistics λ for all test images—A) SPECT images, B) 3DSSP images, C) Z-score images, and D) Z-score of 3DSSP images—were calculated and then a diagnosis was made after applying a fixed threshold value. First, all test images were converted into Fourier amplitude spectra and then channelized with a radial symmetric channeling filter using Eq. 1. The SPECT and Z-score images were performed using a 3D Fourier transform.[25] Because of slice independency, each slice of the 3DSSP and Z-score of 3DSSP images was processed using a 2D Fourier transform, and then Fourier amplitude spectra were summed along axial slices. The continuously distributed λ values of these test statistics for 42 test data (SPECT, Z-score, 3DSSP and Z-score of 3DSSP images) were used for the ROC analysis.

Data analysis

The human observer ratings data and continuously distributed CH observer data were analyzed using the ROCKIT 0.9.1 β program developed by Metz and coworkers (http://xray.bsd.uchicago.edu/krl).[26,27] This program fitted a binormal ROC curve to the given data using a maximum-likelihood technique, and then Az was estimated. Az was used as the measure of comparison between the human and CH observers for the four image types. Especially, correlations between averaged Az of human observer and Az of CH observer for four image types were statistically evaluated using the t-distribution of standardized r (Pearson's correlation coefficient).

RESULTS

Figure 3 shows the profiles of Fourier amplitude spectra for a control and an AD patient for the four types of image. Differences in spectra between AD and controls were quite small for SPECT and 3DSSP images. However, the profiles for controls and AD were quite separable for the Z-scores of the SPECT and 3DSSP images.

Figure 4 shows the ROC curves for SPECT, 3DSSP,

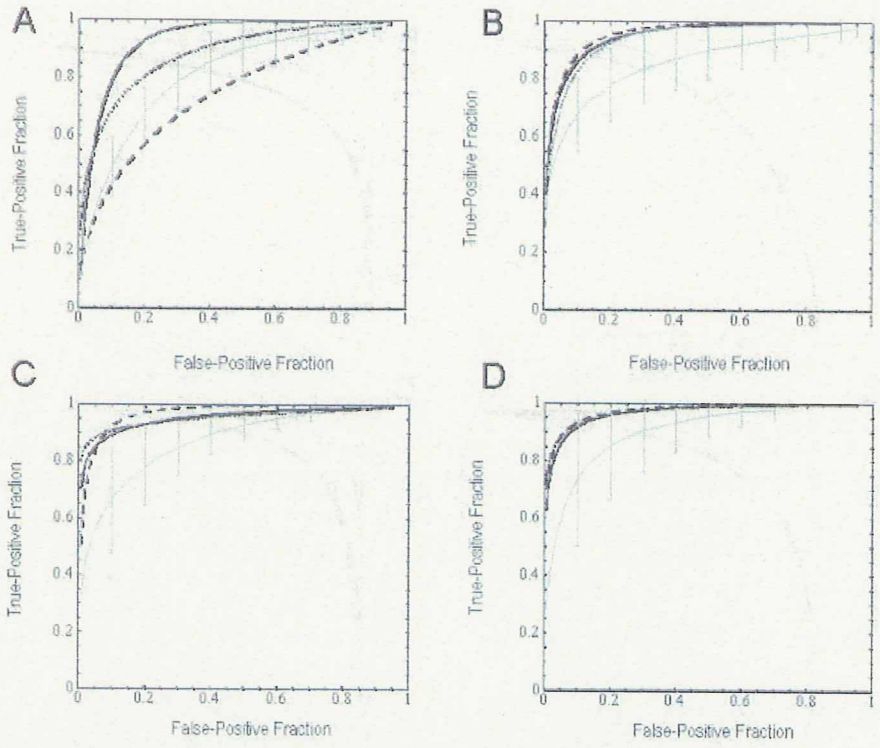

Fig. 5 ROC curves generated by CH observers with low- (*bold solid line*), mid- (*dotted line*), and high- (*dashed line*) channel models, and by averaged physicians (*thin solid lines*) from SPECT images (A), 3DSSP images (B), Z-scores of SPECT images (C) and Z-scores of 3DSSP images.

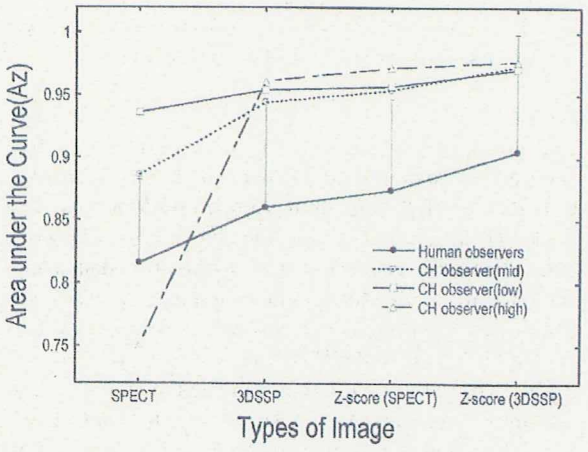

Fig. 6 Comparison of Az obtained by human and CH observers for four types of image. Error bars represent 1 SD for the results from the human observers (n = 5).

Z-score of SPECT, and Z-score of 3DSSP images as interpreted by the five physicians. The average performance of these human observers, as indicated by the average ROC curves, varied with the image type, and was generally better for Z-score images than for SPECT images, and was best for Z-score of 3DSSP images.

Figure 5 shows the ROC curves for SPECT, 3DSSP, Z-score of SPECT, and Z-score of 3DSSP images analyzed by the CH observers using the low-, mid-, and high-ρ_0 channel models in Eq. 1, compared with the averaged curve for the images analyzed by the five physicians. The performance of the CH observer in analyzing the SPECT images (Fig. 5A) was highly dependent on the definition of frequency cutoff values. This dependency was not observed in Figure 5B, C and D for the other image types.

Table 1 and Figure 6 show, respectively, a summary and a comparison of the averaged Az for the four image types as interpreted by the human and CH observers. Significant differences in Az obtained by human observers were observed between SPECT and Z-score of 3DSSP images ($p < 0.05$; paired t-test). CH observers on average performed better than the average human observer, as indicated by the Az values, with the exception of the CH observer that used a high-ρ_0 channel model for the SPECT images. In both groups, similar image-dependent trends were observed; that is, performance generally improved from the original SPECT images to the Z-score images of each respective data set. Pearson's correlation coefficient (r: index of linearity between two variables) for Az for the four image types between the average human and the CH observer using a mid-ρ_0, low-ρ_0 and high-ρ_0, channel model was 0.979, 0.997 and 0.887, respectively. There

Table 1 Summary of diagnostic performance of human observers with ROC analysis and CH observers with three frequency cutoff channel models. For human observers, mean ± 1 SD were calculated among individual Az values of 5 physicians

	SPECT	3DSSP	Z-score	Z-score of 3DSSP
Human observer	0.816 ± 0.066	0.860 ± 0.087	0.874 ± 0.073	0.905 ± 0.094
CHO-Low	0.936	0.954	0.957	0.971
CHO-Mid	0.886	0.944	0.957	0.973
CHO-High	0.750	0.961	0.972	0.977

were significant correlations between CH observer using a mid- and low-ρ_0 and human observers ($p < 0.05$).

DISCUSSION

In this study, we used a CH observer to segregate SPECT perfusion brain images of AD patients from those of controls. The performance of the CH observer was similar to that of the human observers.

The averaged ROC curve obtained by human observers was different among the four types of images shown in Figure 4. Az is 0.816 or 0.905 when either a SPECT image or the Z-score of a 3DSSP image is analyzed. This finding is consistent with that of Honda et al.,[11] who reported that the combined interpretation of the Z-score of a 3DSSP image and the SPECT image elicited an improved Az (0.778) compared with the interpretation of a SPECT image alone (0.679). The absolute values and magnitudes of changes in our study are different from those of Honda et al., perhaps due to differences in patient population (averaged MMSE score: 24 in Honda et al. and 21.6 in our study) and in the experience level of the nuclear medicine physicians.

Figure 5 and 6 show that the rank order of the four types of image processing by the CH observer was similar to that by the human observer. Significant correlations between human and CH observer were observed in condition with mid- and low-ρ_0 channel model. In particular, the performance of the CH observer with the mid-ρ_0 channel model was either close to or within 1 S.D. of human Az. Furthermore, the performance of the CH observer for the SPECT image (Fig. 5A) was heavily dependent on the frequency cutoff; this may be due to the characteristics of the frequency spectra of the SPECT images, which were distributed at the center as shown in Figure 3A.

Physicians focus on test images according to anatomical information and comparison with normal perfusion patterns experienced during previous diagnostic procedures. In contrast, the CH observer identifies frequency patterns on which it bases its inferences. Taking into account this mechanistic difference in image interpretation, the input images for human and CH observers were different in this study. Because statistically processed Z-score images lack anatomical information for the physician's interpretation, the Z-score images were thresholded and superimposed on template MR images (Fig. 2C and D). Additionally, the human observers always read the unprocessed SPECT images together with each processed image in three sessions. On the other hand, the CH observer identifies frequency characteristics and does not require any anatomical information. Therefore, the CH observer was able to work on a test target image alone without any additional information such as the MR template image and the setting of a threshold. The difference in input image for both human and CH observers makes this study unique from previous CH observer studies. Preliminary data suggest that the effects of the superimposed MR image and threshold value were negligible for the performance in the CH observer's analysis of Z-score images (data not shown).

In this study, the CH observer was implemented with 3D or 2D Fourier transformation for volumetric or surface-projection images, respectively. The CH observer with 2D Fourier transformation was originally developed in association with the human visual system on single-slice images.[13] 3D or 2D Fourier transformation with axial summation is used for multislice images[21,25]; however, there is no clear evidence showing any pertinent or obvious benefit of any technique. We assumed that when physicians interpret multislice brain perfusion SPECT images, they generate a mental image of three-dimensional images, and that this human interpretation is associated with 3D data handling. For this reason, we preferred to use 3D Fourier transformation for the multislice CH observer. However, whether 2D or 3D Fourier transformation generates a more accurate representation requires further investigation.[25]

Even though a significant correlation between the human and CH observers was observed, the CH observer with mid-ρ_0 and channel number 5 tends to overestimate the performance compared with the human observer. Another channel number for the CH observer or other numerical observer models, such as channelized non-pre-whitening (CNPW) and non-pre-whitening (NPW) observers,[19] may provide a more accurate prediction of the human observer.

The present approach may be useful for evaluating the effectiveness of a certain image processing technique. The current results suggest that although the SPECT images exhibited such dependence, yielding optimal results for the mid-ρ_0 channel model, statistically processed images may be relatively independent of such models.

However, it is unknown whether the independency of the frequency cutoff channels is observed for other conditions such that the optimization of frequency cutoff channels may be required.

This CH observer model with a frequency cutoff channel can be used to evaluate the effects of partial volume correction on statistically processed or unprocessed SPECT images.[28] Similarly, the effect of scatter correction for relative studies, such as is used in statistical analyses, has not yet been evaluated and may prove to be a useful substrate for further CH observer research.

CONCLUSION

The performance of the CH observer was similar to that of the human observers across all image types. This indicates that CH observer may be useful for evaluating image-processing methods in brain-perfusion SPECT.

ACKNOWLEDGMENTS

This work was supported in part by a Grant-in-Aid for Science Research from the Ministry of Education, Culture, Sports, Science and Technology, research grant 1420061 and a Grant-in-Aid for young researchers from the Association for Nuclear Technology in Medicine.

The authors are grateful to Hayato Odagiri of Tohoku University Hospital and Tachio Sato of IDAC, Tohoku University for data acquisition. The authors are also grateful to Babar Imran of IDAC, Tohoku University for helpful comments about the manuscript and discussion about data processing.

REFERENCES

1. Emilien G, Beyreuther K, Masters CL, Maloteaux JM. Prospects for pharmacological intervention in Alzheimer disease. *Arch Neurol* 2000; 57: 454–459.
2. Donnemiller E, Heilmann J, Wenning GK, Berger W, Decristoforo C, Moncayo R, et al. Brain perfusion scintigraphy with ^{99m}Tc-HMPAO or ^{99m}Tc-ECD and ^{123}I-beta-CIT single photon emission tomography in dementia of the Alzheimer-type and diffuse Lewy body disease. *Eur J Nucl Med* 1997; 24: 320–325.
3. Bonte FJ, Weiner MF, Bigio EH, White CL. Brain blood flow in the dementias: SPECT with histopathologic correlation in 54 patients. *Radiology* 1997; 202: 793–797.
4. Matsuda H. Cerebral blood flow and metabolic abnormalities in Alzheimer's disease. *Ann Nucl Med* 2001; 15: 85–92.
5. Imran MB, Awata S, Kawashima R, Sato K, Ito H, Ono S, et al. Follow-up of improvement in regional cerebral blood flow and mental status in Alzheimer's disease: A case report. *Clinic Nucl Med* 1998; 23: 601–603.
6. Imran MB, Kawashima R, Awata S, Sato K, Kinomura S, Ono S, et al. Parametric Mapping of Cerebral Blood Flow Deficits in Alzheimer's Disease: A SPECT Study Using HMPAO and Image Standardization Technique. *J Nucl Med* 1999; 40: 244–249.
7. Imran MB, Kawashima R, Sato K, Kinomura S, Ono S, Qureshy A, et al. Detection of CBF deficits in neuropsychiatric disorders by an expert system: A ^{99m}Tc-HMPAO brain SPET study using automated image registration. *Nucl Med Comm* 1999; 20: 25–32.
8. El Fakhri G, Kijewski MF, Albert MS, Johnson KA, Moore SC. Quantitative SPECT leads to improved performance in discrimination tasks related to prodromal Alzheimer's disease. *J Nucl Med* 2004; 45: 2026–2031.
9. Ishii K, Sasaki M, Matsui M, Sakamoto S, Yamaji S, Hayashi N, et al. A diagnostic method for suspected Alzheimer's disease using $H_2{}^{15}O$ positron emission tomography perfusion Z score. *Neuroradiology* 2000; 42: 787–794.
10. Imabayashi E, Matsuda H, Asada T, Ohnishi T, Sakamoto S, Nakano S, et al. Superiority of 3-dimensional stereotactic surface projection analysis over visual inspection in discrimination of patients with very early Alzheimer's disease from controls using brain perfusion SPECT. *J Nucl Med* 2004; 45: 1450–1457.
11. Honda N, Machida K, Matsumoto T, Matsuda H, Imabayashi E, Hashimoto J, et al. Three-dimensional stereotactic surface projection of brain perfusion SPECT improves diagnosis of Alzheimer's disease. *Ann Nucl Med* 2003; 17: 641–648.
12. Minoshima S, Frey KA, Koeppe RA, Foster NL, Kuhl DE. A diagnostic approach in Alzheimer's disease using three-dimensional stereotactic surface projection of fluorine-18-FDG PET. *J Nucl Med* 1995; 36: 1238–1248.
13. Myers KJ, Barrett HH. Addition of a channel mechanism to the ideal-observer model. *J Opt Soc Am A* 1987; 4: 2447–2457.
14. Yao J, Barrett HH. Predicting Human Performance by a Channelized Hotelling Observer Model. *Proc SPIE, Mathematical Methods in Medical Imaging* 1992; 1768: 161–168.
15. Barrett HH, Yao J, Rolland JP, Myers KJ. Model observers for assessment of image quality. *Proc Natl Acad Sci USA* 1993; 90: 9758–9765.
16. Qi Y, Tsui BM, Gilland KL, Frey EC, Gullberg GT. Evaluation of Parallel and Fan-Beam Data Acquisition Geometries and Strategies for Myocardial SPECT Imaging. *IEEE Trans Nucl Sci* 2004; 51: 667–672.
17. Farncombe TH, Gifford HC, Narayanan MV, Pretorius PH, Frey EC, King MA. Assessment of Scatter Compensation Strategies for ^{67}Ga SPECT Using Numerical Observers and Human LROC Studies. *J Nucl Med* 2004; 45: 802–812.
18. Sankaran S, Frey EC, Gilland KL, Tsui BM. Optimum Compensation Method and Filter Cutoff Frequency in Myocardial SPECT: A Human Observer Study. *J Nucl Med* 2002; 43: 432–438.
19. Wollenweber SD, Tsui BM, Lalush DS, Frey EC, LaCroix KJ, Gullberg GT. Comparison of Hotelling Observer Models and Human Observers in Defect Detection from Myocardial SPECT Imaging. *IEEE Trans Nucl Sci* 1999; 46: 2098–2103.
20. Gifford HC, King MA, de Vries DJ, Soares EJ. Channelized Hotelling and Human Observer Correlation for Lesion Detection in Hepatic SPECT Imaging. *J Nucl Med* 2000; 41: 514–521.
21. Gifford HC, King MA, Pretorius PH, Wells RG. A Comparison of Human and Model Observers in Multislice LROC Studies. *IEEE Trans Med Img* 2005; 24: 160–169.

22. McKhann C, Drachman D, Folstein M, Katzman R, Price D, Stadlan EM. Clinical diagnosis of Alzheimer's Disease: Report of the NINCDS-ADRDA work group under auspices of Department of Health and Human Services task force on Alzheimer's Disease. *Neurology* 1984; 34: 939–944.
23. Folstein MF, Folstein DE, McHugh PR. "Mini-mental state". A practical method for grading the cognitive state of patients for the clinician. *J Psychiatr Res* 1975; 12: 189–198.
24. Inoue K, Ito H, Shidahara M, Goto R, Kinomura S, Sato K, et al. Database of normal human cerebral blood flow measured by SPECT: II. Quantification of I-123-IMP studies with ARG method and effects of partial volume correction. *Ann Nucl Med* 2006; 20: 139–146.
25. Kim JS, Kinahan PE, Lartizien C, Comtat C, Lewellen TK. A comparison of Planar Versus Volumetric Numerical Observers for Detection Task Performance in Whole-Body PET Imaging. *IEEE Trans Nucl Sci* 2004; 51: 34–40.
26. Metz CE, Herman BA, Shen JH. Maximum-likelihood estimation of ROC curve from continuously-distributed data. *Stat Med* 1998; 17: 1033–1053.
27. Metz CE, Herman BA, Roe CA. Statistical comparison of two ROC curve estimates obtained from partially-paired datasets. *Med Decis Making* 1998; 18: 110–121.
28. Kanetaka H, Matsuda H, Asada T, Ohnishi T, Yamashita F, Imabayashi E, et al. Effects of partial volume correction on discrimination between very early Alzheimer's dementia and controls using brain perfusion SPECT. *Eur J Nucl Med* 2004; 31: 975–980.

Journal of Cerebral Blood Flow & Metabolism (2006), 1–7

www.jcbfm.com

Estimation of oxygen metabolism in a rat model of permanent ischemia using positron emission tomography with injectable ^{15}O-O_2

Takashi Temma[1], Yasuhiro Magata[2], Yuji Kuge[1], Sayaka Shimonaka[1], Kohei Sano[1], Yumiko Katada[1], Hidekazu Kawashima[3], Takahiro Mukai[3], Hiroshi Watabe[4], Hidehiro Iida[4] and Hideo Saji[1]

[1]*Department of Patho-Functional Bioanalysis, Graduate School of Pharmaceutical Sciences, Kyoto University, Kyoto, Japan;* [2]*Laboratory of Genome Bio-Photonics, Photon Medical Research Center, Hamamatsu University School of Medicine, Hamamatsu, Japan;* [3]*Department of Nuclear Medicine and Diagnostic Imaging, Graduate School of Medicine, Kyoto University, Kyoto, Japan;* [4]*Department of Investigative Radiology, National Cardiovascular Center Research Institute, Suita, Japan*

The threshold of cerebral blood flow (CBF) into infarction in rats has been indicated to be similar to that in patients. However, CBF does not reflect metabolic function, and so estimations of oxygen metabolism have been required. Here, we estimated changes in oxygen metabolism after occluding the right middle cerebral artery (MCA) in rats using an injectable ^{15}O-O_2 we developed. A decrease in CBF (left: 0.67±0.22 mL/min/g, right: 0.44±0.17 mL/min/g, $P<0.05$) and compensatory increase in the oxygen extraction fraction (OEF) (left: 0.42±0.13, right: 0.50±0.19, $P<0.05$) were observed at 1-h after occlusion. In contrast, a marked decrease in CBF and the cerebral metabolic rate for oxygen and a collapse of the compensatory OEF mechanism were found at 24 h after occlusion. Injectable ^{15}O-O_2 could be used to reliably estimate oxygen metabolism in an infarction rat model with positron emission tomography.
Journal of Cerebral Blood Flow & Metabolism advance online publication, 22 March 2006; doi:10.1038/sj.jcbfm.9600302

Keywords: OEF; oxygen metabolism; permanent ischemia; positron emission tomography; rat

Introduction

Stroke is closely related to alterations in cerebral blood flow (CBF), the cerebral metabolic rate for oxygen ($CMRO_2$), the oxygen extraction fraction (OEF), cerebral blood volume, and so on while some neurodegenerative disorders such as Alzheimer's disease and Parkinson's disease are also reported to induce a change in CBF (Derejko *et al*, 2001; Mori, 2002) because of tissue degradation. Therefore, estimation of these circulatory and metabolic parameters is important for both pathophysiological studies and the development or evaluation of new methods for treating stroke.

Studies on changes in parameters of cerebral circulation after the onset of stroke have been performed in several animal models (Belayev *et al*, 1997; Ginsberg, 2003; Heiss *et al*, 1997, 1994; Pappata *et al*, 1993; Takamatsu *et al*, 2000; Tenjin *et al*, 1992; Young *et al*, 1996; Zhao *et al*, 1997) and patients (Baron, 2001; Heiss *et al*, 2001). In the studies using larger animals, CBF, OEF and $CMRO_2$ were estimated after the onset of ischemia by positron emission tomography (PET) with ^{15}O-H_2O and ^{15}O-O_2 gas and used as predictors for the progression of brain infarction. These reports indicated that areas showing a decrease in CBF and compensatory increase in OEF in the early phase of stroke were vital several hours after the onset. Also, in studies with rats as an animal model of ischemia, CBF was certainly indicated to be a good predictor for infarction in comparison with the results for

Correspondence: Dr Y Magata, Laboratory of Genome Bio-Photonics, Photon Medical Research Center, Hamamatsu University School of Medicine, 1-20-1 Handayama, Hamamatsu 431-3192, Japan.
E-mail: magata@hama-med.ac.jp
This study was partly supported by Mitsubishi Pharma Research Foundation. This work was also supported by Grants-in-Aid for Scientific Research and by the 21st Century Center of Excellence Program at Kyoto University 'Knowledge Information Infrastructure for Genome Science' and at Hamamatsu University School of Medicine 'Medical Photonics' from the Ministry of Education, Culture, Sports, Science and Technology, Japan.
Received 4 October 2005; revised 7 February 2006; accepted 10 February 2006

patients (Belayev *et al*, 1997; Ginsberg, 2003; Zhao *et al*, 1997). However, CBF does not reflect cell energy metabolism and so measurements of oxygen metabolism are required to accurately estimate tissue viability. Additionally, since that there are functional differences between rodents and humans (Walovitch *et al*, 1994), careful evaluation is needed when using rats to investigate the pathophysiology and progression of human stroke. On these bases, we adopted MCA occluded rats, widely used ischemia model (Kuge *et al*, 1995; Longa *et al*, 1989; Minematsu *et al*, 1992), and evaluated the changes in CBF, OEF and $CMRO_2$ after the onset of stroke with PET.

On the other hand we recently developed a method of measuring regional OEF in the rat brain noninvasively using PET (Magata *et al*, 2003). Here, we designed experiments to estimate CBF, OEF and $CMRO_2$ by PET in the early and late phases of a permanent ischemia in rats.

Materials and methods

Animals

Male Sprague–Dawley rats (250 to 310 g) supplied by Japan SLC Co. (Hamamatsu, Japan) were housed for 1 week under a 12-h light/12-h dark cycle and given free access to food and water. The animal experiments in this study were conducted in accordance with institutional guidelines and approved by the Kyoto University Animal Care Committee.

Preparation of ^{15}O-Labeled Compounds

The production of ^{15}O-H_2O and injection of ^{15}O-oxygen (injectable ^{15}O-O_2) were conducted as reported previously (Magata *et al*, 2003). Briefly, ^{15}O-H_2O was synthesized by the reduction of ^{15}O-O_2 with H_2 gas (catalyzed by Pd black at 140°C) and trapped in a saline solution. As for injectable ^{15}O-O_2, part of an infusion line kit (Terumo Corporation, Tokyo, Japan) used as a blood reservoir and an artificial lung 18 cm in length (Senko Medical Instrument Mfg Co. Ltd, Tokyo, Japan) designed for small animals such as rats were connected to a peristaltic pump (EYELA roller pump RP-1000, Tokyo Rikakikai Co. Ltd, Tokyo, Japan) to make a closed system. Then, 18 to 20 mL of blood was collected from several rats and filtered with saline-wetted gauze. The blood was circulated (100 mL/min) in the system and ^{15}O-O_2 gas (4100 to 5100 MBq/min/500 ml) was introduced into the artificial lung to prepare injectable ^{15}O-O_2 (51 to 90 MBq/ml).

Animal Preparation

Rats were divided into two groups. One was for the early phase PET experiment ($n=7$, 1 h after the onset of occlusion) and the other was for the late phase experiment ($n=6$, 24 h after the onset of occlusion). The rats were starved for 6 h before the operation and anesthetized with chloral hydrate (i.p. 400 mg/kg). For the early phase group, anesthesia was sustained throughout the experiment. The left femoral artery in each rat was catheterized using a PE 20 catheter (i.d. 0.5 mm, o.d. 0.8 mm) for blood sampling during PET study. Then, the right middle cerebral artery (MCA) was occluded intraluminally using a nylon 4-0 monofilament (Kuge *et al*, 1995; Longa *et al*, 1989; Minematsu *et al*, 1992). For the late phase group, each rat was aroused from anesthesia after the right MCA occlusion and then anesthetized for the catheterization of the left femoral artery and PET experiments. After the completion of the operation, rats were administered i.v. with 100 IU of heparin. The animal was placed supine in a stereotaxic apparatus, and its head was restrained by mouth and ear bars. After the acquisition of a blank scan for 180 mins, the apparatus was placed in a PET camera (SHR-7700L, Hamamatsu Photonics, Hamamatsu, Japan) (Watanabe *et al*, 1997). The position was standardized with the aid of a laser beam, and the desired cranial position in the camera was oriented. Rectal temperature was maintained at around 37 °C with the aid of heating pads and blood gases were measured using a blood gas analyzer (Rapidlab 348, Chiron Diagnostics Ltd, Essex, England) several times during the experiment. After the PET experiments, 2,3,5-triphenyltetrazolium chloride (TTC) staining was performed in some cases for evaluating the progression of stroke.

Positron Emission Tomography Experiments

A transmission scan was performed for 30 mins for attenuation correction following the blank scan. Then, a dynamic PET scan was performed using ^{15}O-H_2O (i.v., 148 to 185 MBq) to measure CBF values 1 h or 24 h after the initiation of MCA occlusion. A second PET scan was performed with the administration of injectable ^{15}O-O_2 (i.v., 74 to 148 MBq) over a 60-secs period to measure OEF values after the radioactivity of ^{15}O-H_2O had decayed in the body. In both cases, the total scan acquisition period was 120 secs and the scan consisted of 12×10-second frames. Arterial blood sampling was performed continuously throughout the PET scans and blood centrifugation was also performed for measuring the plasma concentration of ^{15}O radioactivity. The radioactivity of each sample was measured with an NaI well scintillation counter (Packard AutoGamma 500, Packard Instruments, Meriden, CT, USA) calibrated using a ^{22}Na standard radioactive source.

Data Analysis

Positron emission tomography images were obtained as described previously (Magata *et al*, 2003). The rat brain was visualized in four consecutive coronal slices. Then, two regions of interest (ROIs) in each slice, right and left hemispheres, were visually chosen according to the magnetic resonance images obtained previously in the another study using 1.5T MRI. Activity in ROIs was calibrated using a cross calibration factor calculated in

another phantom study with a 10-cm-diameter hollow phantom.

The CBF value in each ROI was calculated by numerically solving the equation (1) as reported previously (Temma *et al*, 2004).

$$R(t) = fA_W(t) * e^{-(f/P+\lambda)t} \quad (1)$$

where the asterisk denotes the convolution integral and other marks are the tissue concentration of ^{15}O radioactivity ($R(t)$), a typical example of that in the late phase experiment is presented in Figure 1, CBF (f), the arterial concentration of ^{15}O-water radioactivity ($A_W(t)$), partition coefficient of water between the brain and blood ($P = 0.8$) and physical decay constant of ^{15}O (λ).

Then, the OEF value was calculated using the same equation (Eq. 2) as that applied to the bolus inhalation of ^{15}O-O_2 gas method (Mintun *et al*, 1984; Shidahara *et al*, 2002), which could be used with this pharmaceutical as shown previously (Magata *et al*, 2003)

$$R(t) = \mathrm{OEF}fA_O(t) * e^{-(f/P+\lambda)t} + fA_W(t) * e^{-(f/P+\lambda)t} + V_B R(1 - V_V' \mathrm{OEF})A_O(t) \quad (2)$$

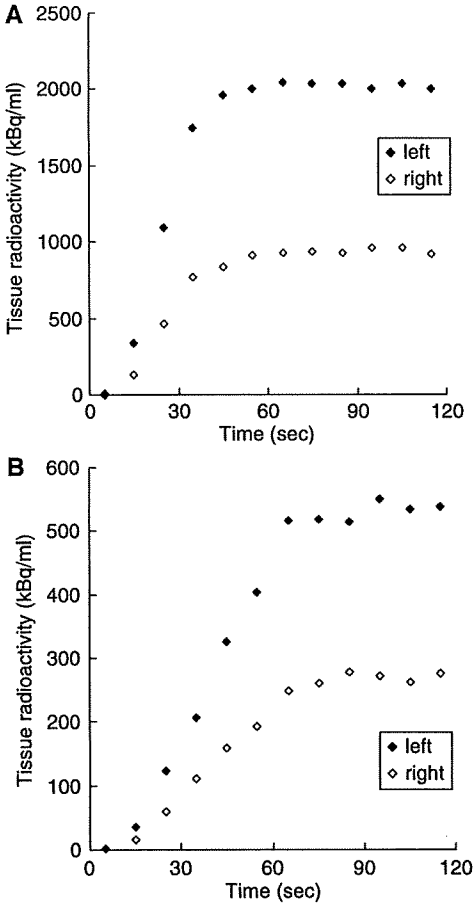

Figure 1 Typical curves of ^{15}O radioactivity obtained by the PET scanning using (**A**) ^{15}O-H_2O and (**B**) injectable ^{15}O-O_2 24 h after the right MCA occlusion.

where the arterial concentration of ^{15}O-O_2 radioactivity ($A_O(t)$), cerebral blood volume ($V_B = 0.04$ mL/g), the hematocrit ratio between central and peripheral regions ($R = 0.85$) and the effective venous ratio in the brain ($V_V' = 0.835$) are used.

The $CMRO_2$ value was calculated using equation (3). In this equation, Hb is gram hemoglobin/mL blood and %Sat is percent saturation of O_2 (Shidahara *et al*, 2002).

$$\mathrm{CMRO_2} = \frac{(1.39 \times \mathrm{Hb} \times \%\mathrm{Sat})}{100} \times \mathrm{OEF} \times \mathrm{CBF} \quad (3)$$

Results

Injectable ^{15}O-O_2 Labeling

The shape of an artificial lung was modified to increase ^{15}O labeling efficiency. Namely, the artificial lung used was three times longer (18 cm) than the previous version while the density of plastic fibers and diameter of the lung were unchanged (Magata *et al*, 2003). In this system, 90 MBq/ml was obtained at maximum.

Physiological Parameters

Blood gases were analyzed several times during the experiment (Table 1). Although several parameters were significantly changed, these changes were slight and levels were not in the abnormal range.

Studies at 1 h After Onset

The relationships between CBF, OEF and $CMRO_2$ at 1 h after the occlusion are shown in scatter diagrams (Figures 2 and 3). As revealed in Figure 2, in the right hemisphere, a decrease in CBF and compensatory increase in OEF were indicated in comparison with the opposite side, inducing a good reciprocal relationship as a whole. Also, the decrease in CBF in the right hemisphere was not so marked. Figure 3 shows the relationship between CBF and $CMRO_2$.

Table 1 Arterial blood gas values before and after PET experiments in MCA occlusion

	1 h		*24 h*	
	Before	*After*	*Before*	*After*
pH	7.32 (0.03)	7.33 (0.03)	7.36 (0.04)	7.35 (0.04)
PO_2 (mm Hg)	97.4 (5.7)	102.8 (10)	94.8 (7.4)	101.5 (4.3)*
PCO_2 (mm Hg)	44.3 (4.2)	39.8 (3.4)	39.7 (4.8)	36.9 (3.7)*
Hct (%)	54.4 (4.8)	51.5 (3.8)*	55 (3.3)	53.5 (3.1)
O_2Sat (%)	96.9 (0.4)	97.2 (0.8)	96.9 (0.7)	97.4 (0.3)*
Hb (g/dl)	18.5 (1.6)	17.5 (1.3)*	18.7 (1.2)	18.2 (1.0)

Statistical differences in each physiological parameter between before and after PET experiments were determined using the Wilcoxon signed-rank test; *$P < 0.05$.
Values listed are means (s.d.).

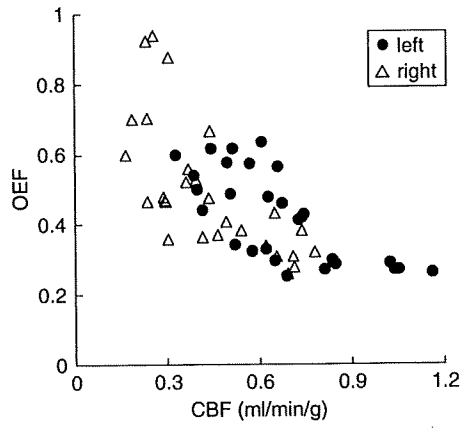

Figure 2 Scatter diagram of CBF (mL/min/g) and OEF values 1 h after the onset of MCA occlusion.

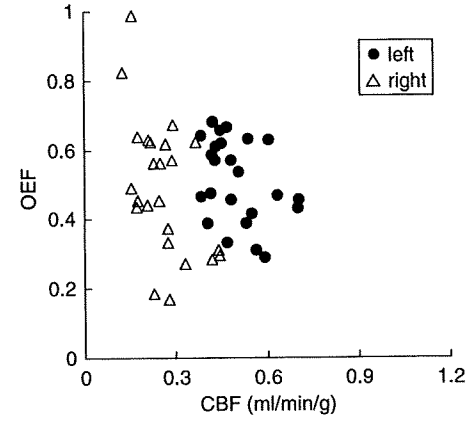

Figure 4 Scatter diagram of CBF (mL/min/g) and OEF values 24 h after the onset of MCA occlusion.

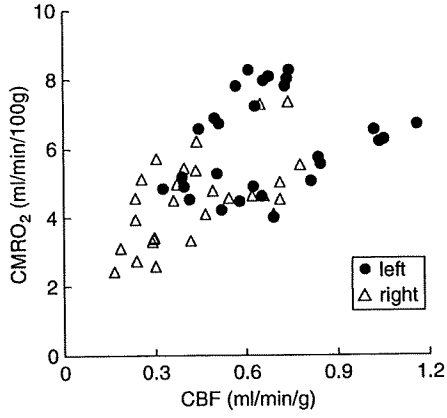

Figure 3 Scatter diagram of CBF (mL/min/g) and $CMRO_2$ (mL/min/100 g) values 1 h after the onset of MCA occlusion.

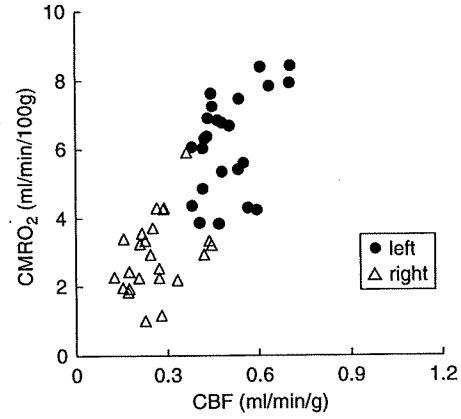

Figure 5 Scatter diagram of CBF (mL/min/g) and $CMRO_2$ (mL/min/100 g) values 24 h after the onset of MCA occlusion.

These two values also exhibit a good correlation, in which the decrease in $CMRO_2$ in the right hemisphere was not so marked.

Studies at 24 h After Onset

The relationships among parameters at 24 h after the occlusion are shown in scatter diagrams (Figures 4 and 5). As shown in Figure 4, in the right hemisphere, the decrease in CBF was more pronounced than at 1 h (Figure 2) and there was no compensatory increase in OEF, resulting in a loss of the good correlation between CBF and OEF. Figure 5 shows the relationship between CBF and $CMRO_2$. The right hemisphere exhibited a marked decrease in $CMRO_2$.

Quantitative Values of Cerebral Blood Flow, Oxygen Extraction Fraction and Cerebral Metabolic Rate for Oxygen

Figure 6 and Table 2 show the averaged hemispheric values of CBF, OEF and $CMRO_2$ at 1 h ($n=7$) and 24 h ($n=6$) after the onset of MCA occlusion. In the right hemisphere at 1 h, the decrease in CBF was not so marked (0.44 ± 0.17 mL/min/g; $P<0.05$ compared with the left side) and a compensatory increase in OEF (0.50 ± 0.19; $P<0.05$ compared with the left side) was observed, inducing a slight decrease in $CMRO_2$ (4.5 ± 1.1 mL/min/100 g; $P<0.05$ compared with the left side). In contrast, at 24 h, there was a marked decrease in CBF (0.26 ± 0.07 mL/min/g, $P<0.05$ compared with both the left side and at 1 h) and no compensatory increase in OEF (0.49 ± 0.19; OEF in the left hemisphere was 0.51 ± 0.12, not significant with each other), resulting in a large decrease in $CMRO_2$ (2.9 ± 0.8 mL/min/100 g; $P<0.05$ compared with both the left side and at 1 h).

Discussion

In our previous report (Magata *et al*, 2003), up to 72 MBq/ml of injectable ^{15}O-O_2 was obtained with

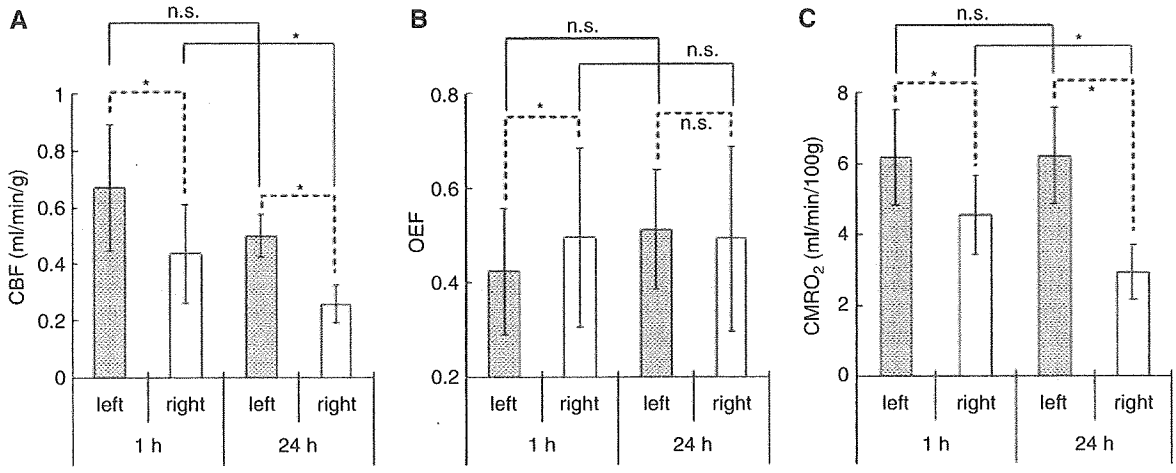

Figure 6 The averaged hemispheric values of (**A**) CBF (mL/min/g), (**B**) OEF and (**C**) $CMRO_2$ (mL/min/100 g) obtained by PET 1 ($n = 7$) and 24 h ($n = 6$) after the onset of MCA occlusion. Significant differences in each parameter (CBF, OEF, $CMRO_2$) between the left and right hemispheres at the same time point and between 1 h and 24 h on the same hemisphere were determined using the Wilcoxon signed-rank test and the Mann–Whitney *U*-test, respectively; $^*P < 0.05$, n.s. not significant.

Table 2 The averaged hemispheric values of CBF (mL/min/g), OEF and $CMRO_2$ (mL/min/100 g) obtained by PET 1 (n = 7) and 24 hours (n = 6) after the onset of MCA occlusion.

	1 h		*24 h*	
	Left	*Right*	*Left*	*Right*
CBF (mL/min/g)	0.67 (0.22)	0.44 (0.17)*	0.50 (0.08)	0.26 (0.07)*,†
OEF	0.42 (0.13)	0.50 (0.19)*	0.51 (0.12)	0.49 (0.19)
$CMRO_2$ (mL/min/100 g)	6.2 (1.3)	4.5 (1.1)*	6.2 (1.4)	2.9 (0.8)*,†

Significant differences in each parameter (CBF, OEF, $CMRO_2$) between the left and right hemispheres at the same time point and between 1 and 24 h on the same hemisphere were determined using the Wilcoxon signed-rank test ($^*P < 0.05$) and the Mann–Whitney *U*-test ($^†P < 0.05$), respectively. Values listed are means (s.d.).

an artificial lung (6 cm length) and about 10 ml of blood. In the present study, the artificial lung was made three times longer to increase the labeling efficiency. First, we used three small artificial lungs connected in series to improve the labeling efficiency. In that system, more blood was needed for summation of the dead volume of each lung, and, the labeling efficiency, radioactivity per unit blood volume, did not increase. Since the total activity in the labeling system is constant if the radioactivity in the supplied gas is constant, highly specific activity of injectable ^{15}O-O_2 can be obtained when a small amount of blood is used. Therefore, the 'long' artificial lung can increase the specific activity of injectable ^{15}O-O_2 owing to the small dead volume. Actually, with this new artificial lung and 18.6 ml of blood, 90 MBq/ml of injectable ^{15}O-O_2 was obtained.

During the experiments, arterial blood gases were analyzed several times (Table 1). At both 1 and 24 h, significant changes were observed in two or three parameters. At 1 h, Hct and Hb decreased after the experiment, indicating slight hemolytic anemia. At 24 h, pO_2, pCO_2 and O_2Sat changed during the PET scans. These values, especially pCO_2, are known to be closely related to the depth of anesthesia and so might reflect a change in the condition of the animal in PET studies. In any case, the changes of these parameters were not so marked and they might not affect the results of experiments.

At 1 h after the onset of MCA occlusion, CBF decreased slightly but significantly in the right hemisphere in comparison with the left side; some ROIs showed normal values and others showed low values (Figure 2). The OEF increased in ROIs with decreased CBF, but not in ROIs with normal CBF (Figure 2). The results indicate that the metabolic compensatory mechanism worked well at 1 h after MCAO. Cerebral metabolic rate for oxygen was also kept in the area of low CBF (Figure 3), and a good correlation between CBF and $CMRO_2$ with a gentle slope was obtained (Figure 3), suggesting that the compensatory mechanism was working well at this time point.

At 24 h after the onset of MCA occlusion, while all ROIs in the right hemisphere showed severely decreased CBF with small variation, OEF showed a

large variation (Figure 4). In the relationship between CBF and $CMRO_2$, all ROIs in the right hemisphere showed severely decreased $CMRO_2$ (Figure 5). These results indicated that the compensatory mechanism at 1 h after MCAO onset had collapsed at 24 h and the progression of ischemic injury was severer than at 1 h.

In Figure 6 and Table 2, quantitative values and standard deviations of CBF, OEF and $CMRO_2$ are summarized. In the right hemisphere, CBF decreased slightly at 1 h and severely at 24 h. Both values were significantly low compared with the opposite sides ($P<0.05$) at both time points and the difference between the 24 h was also significant ($P<0.05$). In the left hemisphere, CBF showed a little decrease but was not significant during 24 h ($P=0.0865$). Since $CMRO_2$ expressed exactly the same values at both time points, the decrease in CBF might not mean a metabolic dysfunction but a vascular disturbance at 24 h. Although blood vessels in the left hemisphere should not be affected directly in our MCAO operation, the progression of the ischemic damage in the right hemisphere included both the spreading of the ischemic core and the disturbance of surrounding blood vessels so that it is considered that the decrease in CBF on the opposite side could have occurred. Furthermore, $CMRO_2$ in the left hemisphere was close to the value obtained previously in normal rats using ^{133}Xe as a CBF tracer and a surgical method for determining OEF (6.3 ± 0.3 mL/min/100 g) (Kozniewska and Szczepanska-Sadowska, 1990). It underlined the preceding discussion that the brain tissue in the left hemisphere was not damaged at all during 24 h and the reason for the little decrease in CBF was vascular disturbance.

In the right hemisphere, $CMRO_2$ decreased severely during 24 h in the same manner as CBF (Figure 6, Table 2). Since these values did not represent $CMRO_2$ in the ischemic core but just values in the entire right hemisphere because of the large size of ROIs, it is difficult to discuss the progression of impairment. However, taken together with the decreases in CBF in both hemispheres during 24 h, the decrease in $CMRO_2$ might not mean an ischemic core-specific progression of tissue disturbance but a spreading of the ischemic damage throughout the hemisphere. In fact, TTC staining revealed no sign of disturbance at 1 h but severe disruption at 24 h in the right hemisphere.

Meanwhile, an obvious change of OEF was also evident during 24 h (Figure 6, Table 2). The increase in OEF in the right hemisphere compared with the left side at 1 h after the onset of MCAO ($P<0.05$) showed that the metabolic compensatory mechanism was working well. However, at 24 h, the OEF was the same in both hemispheres ($P=0.7532$), which indicates that the compensatory mechanism did not function at 24 h after the onset. Therefore, considering that the condition in the left hemisphere at 1 h was actually normal or stage I in the course of the ischemic disorder (Nemoto *et al*, 2004; Powers, 1991), the right hemisphere at 1 h might include partly stage II and stage III (Figures 2 and 3; CBF was normal or decreased, OEF increased and $CMRO_2$ was normal or slightly decreased), the left hemisphere at 24 h might be expressed at stage II (Figures 4 and 5; CBF decreased, OEF increased, $CMRO_2$ was normal) and the right hemisphere at 24 h might include early and severe phases of stage III (Figures 4 and 5; CBF decreased, OEF increased or decreased and $CMRO_2$ strikingly decreased).

Conclusion

In this paper, we estimated the changes in CBF, OEF and $CMRO_2$ after the onset of MCA occlusion in rats by PET using injectable ^{15}O-O_2. In the early phase after occlusion, a decrease in CBF and compensatory increase in OEF were shown, and in contrast, CBF and $CMRO_2$ were severely decreased in the late phase. This is the first report to indicate reliable oxygen metabolism in a MCAO rat model using PET.

References

Baron JC (2001) Perfusion thresholds in human cerebral ischemia: historical perspective and therapeutic implications. *Cerebrovasc Dis* 11(Suppl 1):2–8

Belayev L, Zhao W, Busto R, Ginsberg MD (1997) Transient middle cerebral artery occlusion by intraluminal suture: I. Three-dimensional autoradiographic image-analysis of local cerebral glucose metabolism–blood flow interrelationships during ischemia and early recirculation. *J Cereb Blood Flow Metab* 17:1266–80

Derejko M, Slawek J, Lass P, Nyka WM (2001) Cerebral blood flow changes in Parkinson's disease associated with dementia. *Nucl Med Rev Cent East Eur* 4:123–7

Ginsberg MD (2003) Adventures in the pathophysiology of brain ischemia: penumbra, gene expression, neuroprotection: the 2002 Thomas Willis Lecture. *Stroke* 34:214–23

Heiss WD, Graf R, Lottgen J, Ohta K, Fujita T, Wagner R *et al* (1997) Repeat positron emission tomographic studies in transient middle cerebral artery occlusion in cats: residual perfusion and efficacy of postischemic reperfusion. *J Cereb Blood Flow Metab* 17:388–400

Heiss WD, Graf R, Wienhard K, Lottgen J, Saito R, Fujita T *et al* (1994) Dynamic penumbra demonstrated by sequential multitracer PET after middle cerebral artery occlusion in cats. *J Cereb Blood Flow Metab* 14:892–902

Heiss WD, Kracht LW, Thiel A, Grond M, Pawlik G (2001) Penumbral probability thresholds of cortical flumazenil binding and blood flow predicting tissue outcome in patients with cerebral ischaemia. *Brain* 124:20–9

Kozniewska E, Szczepanska-Sadowska E (1990) V2-like receptors mediate cerebral blood flow increase following vasopressin administration in rats. *J Cardiovasc Pharmacol* 15:579–85

Kuge Y, Minematsu K, Yamaguchi T, Miyake Y (1995) Nylon monofilament for intraluminal middle cerebral artery occlusion in rats. *Stroke* 26:1655–8

Longa EZ, Weinstein PR, Carlson S, Cummins R (1989) Reversible middle cerebral artery occlusion without craniectomy in rats. *Stroke* 20:84–91

Magata Y, Temma T, Iida H, Ogawa M, Mukai T, Iida Y *et al* (2003) Development of injectable O-15 oxygen and estimation of rat OEF. *J Cereb Blood Flow Metab* 23: 671–6

Minematsu K, Li L, Fisher M, Sotak CH, Davis MA, Fiandaca MS (1992) Diffusion-weighted magnetic resonance imaging: rapid and quantitative detection of focal brain ischemia. *Neurology* 42:235–40

Mintun MA, Raichle ME, Martin WR, Herscovitch P (1984) Brain oxygen utilization measured with O-15 radiotracers and positron emission tomography. *J Nucl Med* 25:177–87

Mori S (2002) Responses to donepezil in Alzheimer's disease and Parkinson's disease. *Ann NY Acad Sci* 977: 493–500

Nemoto EM, Yonas H, Kuwabara H, Pindzola RR, Sashin D, Meltzer CC *et al* (2004) Identification of hemodynamic compromise by cerebrovascular reserve and oxygen extraction fraction in occlusive vascular disease. *J Cereb Blood Flow Metab* 24:1081–9

Pappata S, Fiorelli M, Rommel T, Hartmann A, Dettmers C, Yamaguchi T *et al* (1993) PET study of changes in local brain hemodynamics and oxygen metabolism after unilateral middle cerebral artery occlusion in baboons. *J Cereb Blood Flow Metab* 13: 416–24

Powers WJ (1991) Cerebral hemodynamics in ischemic cerebrovascular disease. *Ann Neurol* 29:231–40

Shidahara M, Watabe H, Kim KM, Oka H, Sago M, Hayashi T *et al* (2002) Evaluation of a commercial PET tomograph-based system for the quantitative assessment of rCBF, rOEF and $rCMRO_2$ by using sequential administration of ^{15}O-labeled compounds. *Ann Nucl Med* 16:317–27

Takamatsu H, Tsukada H, Kakiuchi T, Nishiyama S, Noda A, Umemura K (2000) Detection of reperfusion injury using PET in a monkey model of cerebral ischemia. *J Nucl Med* 41:1409–16

Temma T, Magata Y, Mukai T, Kitano H, Konishi J, Saji H (2004) Availability of *N*-isopropyl-p-[(125)I]iodoamphetamine (IMP) as a practical cerebral blood flow (CBF) indicator in rats. *Nucl Med Biol* 31:811–4

Tenjin H, Ueda S, Mizukawa N, Imahori Y, Hino A, Ohmori Y *et al* (1992) Positron emission tomographic measurement of acute hemodynamic changes in primate middle cerebral artery occlusion. *Neurol Med Chir (Tokyo)* 32:805–10

Walovitch RC, Cheesman EH, Maheu LJ, Hall KM (1994) Studies of the retention mechanism of the brain perfusion imaging agent 99mTc-bicisate (99mTc-ECD). *J Cereb Blood Flow Metab* 14(Suppl 1):S4–11

Watanabe M, Okada H, Shimizu K, Omura T, Yoshikawa E, Kosugi T *et al* (1997) A high resolution animal PET scanner using compact PS-PMT detectors. *IEEE Trans Nucl Sci* 44:1277–82

Young AR, Sette G, Touzani O, Rioux P, Derlon JM, MacKenzie ET *et al* (1996) Relationships between high oxygen extraction fraction in the acute stage and final infarction in reversible middle cerebral artery occlusion: an investigation in anesthetized baboons with positron emission tomography. *J Cereb Blood Flow Metab* 16:1176–88

Zhao W, Belayev L, Ginsberg MD (1997) Transient middle cerebral artery occlusion by intraluminal suture: II. Neurological deficits, and pixel-based correlation of histopathology with local blood flow and glucose utilization. *J Cereb Blood Flow Metab* 17:1281–90

Annals of Nuclear Medicine Vol. 20, No. 9, 583–588, 2006

PET kinetic analysis—compartmental model

Hiroshi WATABE,* Yoko IKOMA,** Yuichi KIMURA,*** Mika NAGANAWA***,**** and Miho SHIDAHARA**

*Department of Investigative Radiology, National Cardiovascular Center Research Institute
**Department of Biophysics, Molecular Imaging Center, National Institute of Radiological Sciences
***Positron Medical Center, Tokyo Metropolitan Institute of Gerontology
****Japan Society for the Promotion of Science

PET enables not only visualization of the distribution of radiotracer, but also has ability to quantify several biomedical functions. Compartmental model is a basic idea to analyze dynamic PET data. This review describes the principle of the compartmental model and categorizes the techniques and approaches for the compartmental model according to various aspects: model design, experimental design, invasiveness, and mathematical solution. We also discussed advanced applications of the compartmental analysis with PET.

Key words: PET, compartmental model, pharmacokinetics

1. Introduction

RECENTLY, positron emission tomography (PET) imaging with ^{18}F labeled fluorodeoxyglucose (FDG) has shown great success in tumor detection and cancer staging. Furthermore, PET has been widely accepted as a tool for "molecular imaging," which is regarded as the main paradigm for twenty-first century biology.[1–3] Among several imaging modalities (such as MRI, SPECT, optical imaging) for molecular imaging, PET imaging has several advantages such as high sensitivity and ability for quantitative measurement. However, in order to exploit PET's potential fully, one must understand some basic principles behind PET. Data measured by PET camera are composed of various signals. In order to isolate the component of the signal of interest, a mathematical framework has been developed by several investigators. "Compartmental model" originated from the field of pharmacokinetics and is a commonly used mathematical model for analyzing PET data. Many methods to analyze PET data have been developed based on the compartmental model including the quantification of blood flow,[4] cerebral metabolic rate for glucose,[5] cerebral oxygen utilization[6] and neuroreceptor ligand binding.[7] In this review, the concept of the compartmental model with PET is introduced and several applications by the compartmental model and PET are discussed.

Received October 2, 2006, revision accepted October 2, 2006.

For reprint contact: Hiroshi Watabe, Ph.D., Department of Investigative Radiology, National Cardiovascular Center Research Institute, 5–7–1 Fujishiro-dai, Suita, Osaka 565–8565, JAPAN.

E-mail: watabe@ri.ncvc.go.jp

2. General concepts for compartmental model to analyze PET data

In a typical PET study, PET data are sequentially obtained after the radioactive tracer is introduced (usually administrated intravenously) over time. By applying proper corrections for attenuation, dead-time of detector, physical decay of radioactivity and scattered photons, PET data represent the tracer concentration (Bq/m*l*) at a certain time. In order to interpret the observed PET data over time, we assume there are physiologically separate pools of tracer substance as "compartments." Figure 1 represents general four compartments model or three tissue compartments model. The first compartment is the arterial blood. From arterial blood, the radioligand passes into the second compartment, known as the free compartment. The third compartment is the region of specific binding which we are usually interested to observe. The fourth compartment is a nonspecific-binding compartment that exchanges with the free compartment. The transport and binding rates of the tracer (K_1 [m*l*$\cdot$g$^{-1}\cdot$min^{-1}], k_2 [min^{-1}], k_3 [min^{-1}], k_4 [min^{-1}], k_5 [min^{-1}] and k_6 [min^{-1}] in Fig. 1) are assumed to be linearly related

to the concentration differences between two compartments, and the following differential equations are described at time t [min].

$$\frac{dC_b(t)}{dt} = k_3C_f(t) - k_4C_b(t)$$

$$\frac{dC_f(t)}{dt} = K_1C_p(t) + k_6C_n(t) + k_4C_b(t) - (k_2 + k_3 + k_5)C_f(t)$$

$$\frac{dC_n(t)}{dt} = k_5C_f(t) - k_6C_n(t) \qquad (1)$$

where $C_p(t)$, $C_f(t)$, $C_b(t)$ and $C_n(t)$ are radioactivity concentrations at time t [min] for each compartment. Data obtained by PET camera ($C_{PET}(t)$) are a summation of these compartments as

$$C_{PET}(t) = C_f(t) + C_b(t) + C_n(t) \qquad (2)$$

The parameters can be estimated by fitting the model to measured PET data with arterial radioactivity concentration ($C_p(t)$) as input function. The $C_p(t)$ must be measured separately from PET data acquisition. The frequent manual sampling of the arterial blood or continuous radioactivity monitoring by external radiation detector[8,9] is required (there are several techniques to avoid blood sampling, which will be discussed later).

It is sometimes more useful to employ combinations of the parameters as "macro parameter" to represent the observed data rather than individual parameter. The frequently used macro parameters are distribution volume (K_1/k_2), and binding potential ($\frac{K_1k_3}{k_2k_4}$ or $\frac{k_3}{k_4}$). These estimated parameters or the macro parameters provide several useful pieces of information such as the behavior of target molecule, physiological function, and pharmacokinetics.

There are several assumptions that underlay the compartmental model to interpret PET data. Physiological process and molecular interactions are not influenced by injected radioligand and should be constant during PET measurement. Because PET imaging has sensitivity of 10^{-11}–10^{-12} mol/l, most PET studies fulfill this assumption. We presume that each compartment is homogeneous and the radioligand that passes from one compartment to the other is instantaneously mixed in the compartment.

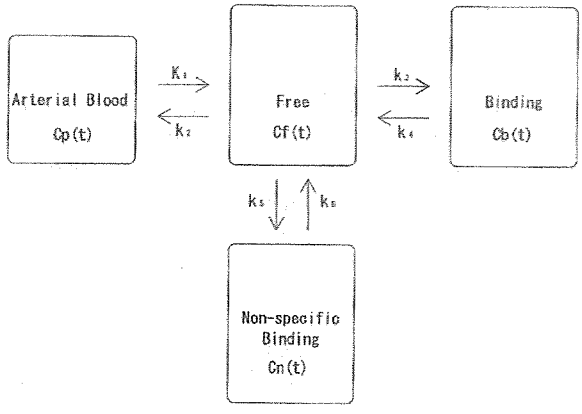

Fig. 1 General three tissue (or four-compartments) compartmental model. This model consists of components of plasma, free ligand in tissue, specific binding and non-specific binding and six rate constants (K_1–k_6).

3. Classification of the compartmental models and analyzes

Many compartmental models and many methods have been proposed to analyze PET data. In this section, we classify the models and methods in different aspects.

3.1 Number of the compartments

The answer for how many compartments must be considered depends on the chemical and biological properties of the radioligand. Moreover, the three tissue compartmental model in Figure 1 has six parameters and the statistical quality of the observed PET data or the statistical properties of the defined model often does not allow to estimate six parameters at once. By reducing the number of the compartments, the number of estimated parameters is reduced and the statistical variability of the parameters is suppressed.

The simplest compartmental model is the model which has only one tissue compartment (Fig. 2). The most popular application of the single-tissue compartment is blood flow measurement by ^{15}O labeled water and PET based on the Fick principle.[4] The single-tissue compartmental model is sometimes enough for many radioligands to describe their kinetics. The neuroreceptor ligand actually behaves under the two or three tissue compartmental model; however, practically one tissue compartmental model is sufficient to describe the kinetics of the ligand in some cases.[10,11]

The two tissue compartmental model (Fig. 3) fits many radioligand tracers well. [^{18}F]FDG is a typical example of the two tissue compartmental model. For many neuroreceptor radioligands, rapid equilibrium between the nonspecific-binding and free compartments can be assumed and the two tissue compartmental model is enough to interpret the kinetics of the ligand.

If the injected radioligand is metabolized and the me-

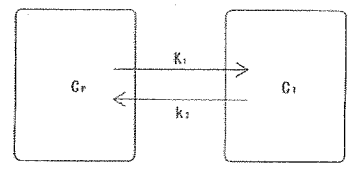

Fig. 2 Single tissue compartmental model. This model has only one compartment in tissue and exchange radiotracer between plasma compartment (C_P) and tissue compartment (C_T) by two rate constants K_1 and k_2.

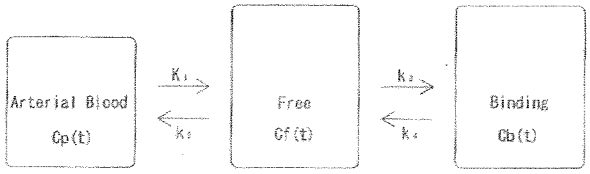

Fig. 3 Two tissue (or three-compartments) compartmental model. This model consists of components of plasma, free ligand (plus non-specific binding) in tissue and specific binding and four rate constants (K_1–k_4).

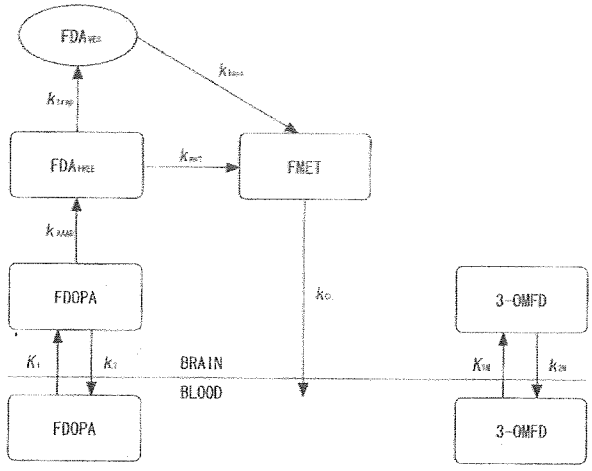

Fig. 4 Compartmental model of FDOPA metabolism.[12] The model consists of FDOPA, fluorodopamine (FDA), FDA metabolites (FMET consist of [^{18}F]6-fluoro-L-3,4-dihydroxyphenylacetic acid, [^{18}F]6-fluorohomovanillic acid) and 3-*O*-methyl-fluorodopa (3-OMFD).

tabolized compounds are detectable by the PET camera, the compartmental model must take into account the kinetics of the metabolites, which results in more compartments and parameters to be estimated. [^{18}F]6-fluoro-L-dopa (FDOPA) is a typical example of these kinds of radioligands (See Fig. 4).[12]

Alternatively, there are several approaches which do not require assumption of the number of compartments. Instead, they estimate the macro parameters such as the distribution volume based on common properties among the compartmental models. Graphical approaches by Patlak et al.[13] and Logan et al.[14] estimate the macro parameter by graphically fitting a straight line to the transformed experimental data. Spectral analysis[15,16] assumes that the observed PET data can be described by sets of exponentials as impulse response function and employs non-negative least squares fitting to estimate exponential basis functions. The spectral analysis also supplies information on the number of compartments. The basis pursuit denosing[17] extends the concept of the spectral analysis and permits negative coefficient for the basis functions, facilitating adaptation for the reference tissue model (see below for explanation of the reference tissue model).

3.2 Bolus or infusion administration of the radiotracer

In many cases, the radiotracer is administrated as a bolus, and dynamic changes of PET data are observed and analyzed. As shown in Eq. 1, the compartmental model mathematically includes differential equations. If equilibrium condition is achieved, i.e. the change rate of the concentration against time in the compartment is zero, the left side of Eq. 1 becomes zero, which simplifies mathematical formulations for the compartmental analysis. Continuously supplying radiotracer may produce equilibrium condition. Well established technique using this strategy is measurements of cerebral blood flow and oxygen consumption by continuous inhalations of ^{15}O–CO, ^{15}O–CO_2 and ^{15}O–O_2 gases.[18] Another example of usage of the equilibrium condition is bolus plus constant infusion paradigm for neuroreceptor study.[19] This experimental paradigm starts with bolus injection of the radiotracer followed by continuously infused administration of the radiotracer to achieve constant concentrations in the tissue and blood. The distribution volume and binding potential can be easily obtained by calculating ratios between the radioactivity concentrations in the tissues and blood. The rate of the infusion may vary between subjects, and optimal scheduling of the experiments must be sought for success of the bolus plus infusion paradigm.[20]

3.3 Compartmental analysis with the arterial input function or without the arterial input function

As described above, the arterial radioactivity curve as the input curve is essential for the compartmental analysis with PET. However, arterial sampling is invasive and technically demanding. If the heart chamber is inside the field-of-view of PET camera, the arterial input function can be directly derived from PET images.[21,22] Or the input function is estimated by extracting components of blood from PET images by means of image-processing.[23,24]

Alternatively, several techniques based on compartmental analysis have been developed. A common strategy for these techniques is omitting the arterial input function by assuming that all pixels of the interest in the PET data share the same arterial input function.[25–28] Many radioligands for neuroreceptor use the reference tissue model (Fig. 5) of Lammertsma et al.[27] or its extensions.[29] Although these techniques have several advantages over the method with the arterial input function, especially non-invasiveness, these techniques generally have more assumptions and need caution for use. For example, the existence of the specific binding in the reference region result in an underestimation of specfic binding in the target region.[30]

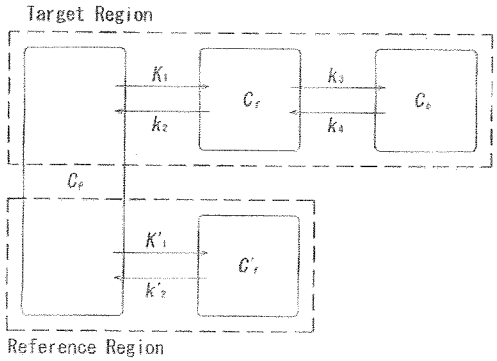

Fig. 5 Reference tissue model.[27] The target region and the reference region have the same plasma input function. It uses the C'_f, time activity curve of the reference region as an indirect input function.

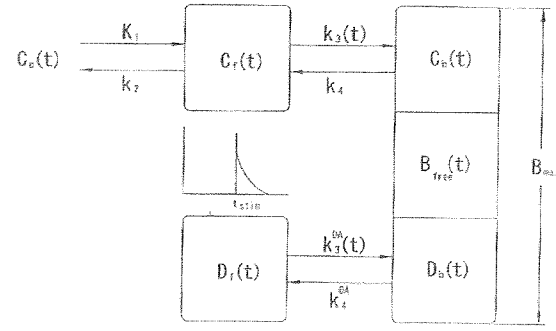

Fig. 6 Extended receptor model which accounts for dopamine competition.[37] Amphetamine is introduced at time t_{stim}, and endogenous dopamine is released. The parameter k_3 is varied according to free receptor B_{free}.

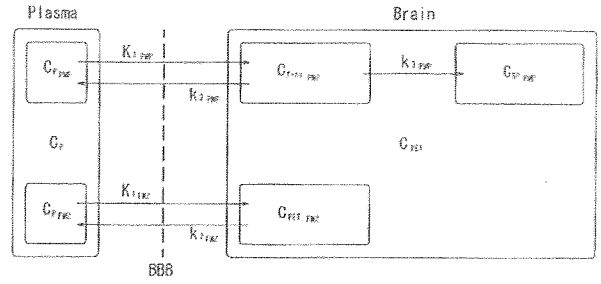

Fig. 7 Combined compartmental model for dual injections of PMP and DTBZ or FMZ.[38]

3.4 Non-linear or linear fitting

In order to estimate parameters from Eqs. 1 and 2, non-linear least squares fitting procedure is required. Generally, the non-linear fitting procedure is computationally expensive. Several graphical approaches[13,14,31,32] are available to make non-linear problems into linear ones, which results in quick estimation of parameters. One must select the proper graphical approach for a particular radiotracer. For instance, Patlak plot[13] must be applied for irreversible tracer and Logan plot[14] for reversible tracer. The statistical bias may be introduced due to noise in PET data, and the improper selection of the graphical approach leads to wrong parameter estimation.[32,33] Basis function approach[34,35] is another major method for linearization. In this approach, non-linear terms of solution for the compartmental model are discretely precalculated within available ranges of the kinetic parameters, which results in a linear system to solve. Although the method is computationally more demanding than the graphical approaches, the method allows determination of the individual kinetic parameters of the model.

4. Advanced applications using the compartmental analysis

As mentioned above, the compartmental model assumes that kinetic parameters are constant during the experiment. By intentionally violating this assumption, however, PET can detect and quantify transient changes in neurotransmitter concentrations.[36] Endres et al.[37] extended the compartmental model to consider endogenous dopamine release (Fig. 6) and showed that PET data were well fitted to the model.

Recently, there has been growing interest in detecting multiple functions simultaneously within the same subject by multiple injections of radiotracer. Koeppe et al.[38] developed a combined compartmental model (Fig. 7) and studied dual injections of [^{11}C]flumazenil (FMZ), *N*-[^{11}C]methylpiperidinyl propionate (PMP) and [^{11}C]dihydrotetrabenazine (DTBZ). Kudomi et al.[39] developed a model which compensates for the background radioactivity from a previously injected radiotracer and computes CBF and $CMRO_2$ from a single PET acquisition with a sequential administration of [^{15}O]O_2 and [^{15}O]H_2O.

As molecular imaging, many trials are currently underway to image reporter gene expression *in vivo* using PET. The compartmental model can play a role to quantify kinetics of the reporter protein. Green et al.[40] showed that the kinetics of ^{18}F-FHBG can be represented by a two-tissue compartmental model, and k_3 is an index of activity of the reporter protein. However, there are still several issues remaining for quantification of therapeutic gene expression[41] and further investigations are required. One particular problem is that the time scale observed by PET may differ from that for gene expression.

5. Conclusion

The compartmental model is a basic concept to quantitatively evaluate PET data. Many techniques based on the compartmental model have been developed as described in this review and one must select the most appropriate technique to analyze one's own PET data. In future, the

compartmental model will play an important role in molecular imaging.

REFERENCES

1. Luker G, Piwnica-Worms D. Molecular imaging *in vivo* with PET and SPECT. *Acad Radiol November* 2001; 8: 4–14.
2. Dobrucki L, Sinusas A. Molecular imaging. A new approach to nuclear cardiology. *Q J Nucl Med Mol Imaging* 2005; 49 (1): 106–115.
3. Weissleder R. Molecular imaging in cancer. *Science* 2006; 312 (5777): 1168–1171.
4. Kety S. The theory and applications of the exchange of inert gas at the lungs and tissues. *Pharmacol Rev* 1951; 3: 3–41.
5. Reivich M, Kuhl D, Wolf A, Greenberg J, Phelps M, Ido T, et al. The [^{18}F]fluorodeoxyglucose method for the measurement of local cerebral glucose utilization in man. *Circ Res* 1979; 44 (1): 127–137.
6. Mintun M, Raichle M, Martin W, Herscovitch P. Brain oxygen utilization measured with O-15 radiotracers and positron emission tomography. *J Nucl Med* 1984; 25 (2): 177–187.
7. Mintun M, Raichle M, Kilbourn M, Wooten G, Welch M. A quantitative model for the *in vivo* assessment of drug binding sites with positron emission tomography. *Ann Neurol* 1984; 15 (3): 217–227.
8. Eriksson L, Holte S, Bohm C, Kesselberg M, Hovander B. Automated blood sampling systems for positron emission tomography. *IEEE Nucl Sci* 1988; 35 (1): 703–707.
9. Kudomi N, Choi E, Yamamoto S, Watabe H, Kim K, Shidahara M, et al. Development of a GSO detector assembly for a continuous blood sampling system. *IEEE Trans Nucl Sci* 2003; 50 (1): 70–73.
10. Koeppe R, Holthoff V, Frey K, Kilbourn M, Kuhl D. Compartmental analysis of [^{11}C]flumazenil kinetics for the estimation of ligand transport rate and receptor distribution using positron emission tomography. *J Cereb Blood Flow Metab* 1991; 11 (5): 735–744.
11. Watabe H, Channing M, Der M, Adams H, Jagoda E, Herscovitch P, et al. Kinetic analysis of the 5-HT2A ligand [^{11}C]MDL 100,907. *J Cereb Blood Flow Metab* 2000; 20 (6): 899–909.
12. Endres C, Endres C, DeJesus O, DeJesus O, Uno H, Uno H, et al. Time profile of cerebral [^{18}F]6-fluoro-L-DOPA metabolites in nonhuman primate: implications for the kinetics of therapeutic L-DOPA. *Front Biosci* 2004; 9: 505–512.
13. Patlak C, Blasberg R. Graphical evaluation of blood-to-brain transfer constants from multiple-time uptake data. Generalizations. *J Cereb Blood Flow Metab* 1985; 5 (4): 584–590.
14. Logan J, Fowler J, Volkow N, Wolf A, Dewey S, Schlyer D, et al. Graphical analysis of reversible radioligand binding from time-activity measurements applied to *N*-[^{11}C]methyl-(–)-cocaine PET studies in human subjects. *J Cereb Blood Flow Metab* 1990; 10 (5): 740–747.
15. Cunningham V, Jones T. Spectral analysis of dynamic PET studies. *J Cereb Blood Flow Metab* 1993; 13 (1): 15–23.
16. Murase K. Spectral analysis: principle and clinical applications. *Ann Nucl Med* 2003; 17 (6): 427–434.
17. Gunn R, Gunn S, Turkheimer F, Aston J, Cunningham V. Positron emission tomography compartmental models: a basis pursuit strategy for kinetic modeling. *J Cereb Blood Flow Metab* 2002; 22 (12): 1425–1439.
18. Lammertsma A, Jones T, Frackowiak R, Lenzi G. A theoretical study of the steady-state model for measuring regional cerebral blood flow and oxygen utilisation using oxygen-15. *J Comput Assist Tomogr* 1981; 5 (4): 544–550.
19. Carson R, Channing M, Blasberg R, Dunn B, Cohen R, Rice K, et al. Comparison of bolus and infusion methods for receptor quantitation: application to [^{18}F]cyclofoxy and positron emission tomography. *J Cereb Blood Flow Metab* 1993; 13 (1): 24–42.
20. Watabe H, Endres C, Breier A, Schmall B, Eckelman W, Carson R. Measurement of dopamine release with continuous infusion of [^{11}C]raclopride: optimization and signal-to-noise considerations. *J Nucl Med* 2000; 41 (3): 522–530.
21. Iida H, Kanno I, Takahashi A, Miura S, Murakami M, Takahashi K, et al. Measurement of absolute myocardial blood flow with $H_2{}^{15}O$ and dynamic positron-emission tomography. Strategy for quantification in relation to the partial-volume effect. *Circulation* 1988; 78 (1): 104–115.
22. Choi Y, Huang S, Hawkins R, Kim J, Kim B, Hoh C, et al. Quantification of myocardial blood flow using ^{13}N-ammonia and PET: comparison of tracer models. *J Nucl Med* 1999; 40 (6): 1045–1055.
23. Watabe H, Channing M, Riddell C, Jousse F, Libutti S, Carrasquillo J, et al. Noninvasive estimation of the aorta input function for measurement of tumor blood flow with [^{15}O]water. *IEEE Trans Med Imaging* 2001; 20 (3): 164–174.
24. Naganawa M, Kimura Y, Ishii K, Oda K, Ishiwata K, Matani A. Extraction of a plasma time-activity curve from dynamic brain PET images based on independent component analysis. *IEEE Trans Biomed Eng* 2005; 52 (2): 201–210.
25. Watabe H, Itoh M, Cunningham V, Lammertsma A, Bloomfield P, Mejia M, et al. Noninvasive quantification of rCBF using positron emission tomography. *J Cereb Blood Flow Metab* 1996; 16 (2): 311–319.
26. Bella ED, Clackdoyle R, Gullberg G. Blind estimation of compartmental model parameters. *Phys Med Biol* 1999; 44 (3): 765–780.
27. Lammertsma A, Bench C, Hume S, Osman S, Gunn K, Brooks D, et al. Comparison of methods for analysis of clinical [^{11}C]raclopride studies. *J Cereb Blood Flow Metab* 1996; 16 (1): 42–52.
28. Lammertsma A, Hume S. Simplified reference tissue model for PET receptor studies. *Neuroimage* 1996; 4 (3 Pt 1): 153–158.
29. Endres C, Bencherif B, Hilton J, Madar I, Frost J. Quantification of brain muopioid receptors with [^{11}C]carfentanil: reference-tissue methods. *Nucl Med Biol* 2003; 30 (2): 177–186.
30. Kropholler MA, Boellaard R, Schuitemaker A, Folkersma H, Berckel BNMV, Lammertsma AA. Evaluation of reference tissue models for the analysis of [^{11}C](R)-PK11195 studies. *J Cereb Blood Flow Metab* 2006.
31. Yokoi T, Iida H, Itoh H, Kanno I. A new graphic plot analysis for cerebral blood flow and partition coefficient with iodine-123-iodoamphetamine and dynamic SPECT